

Dynamic modulation in graphene-integrated silicon photonic crystal nanocavity

Long-Pan Wang(汪陇盼), Cheng Ren(任承), De-Zhong Cao(曹德忠), Rui-Jun Lan(兰瑞君), and Feng Kang(康凤)
Citation: Chin. Phys. B, 2021, 30 (**6**): 064209. DOI: 10.1088/1674-1056/abda2b
Journal homepage: http://cpb.iphy.ac.cn; http://iopscience.iop.org/cpb

What follows is a list of articles you may be interested in

Graphene-tuned threshold gain to achieve optical pulling force on microparticle

Hong-Li Chen(陈鸿莉), and Yang Huang(黄杨)
Chin. Phys. B, 2021, 30 (**6**): 064205. DOI: 10.1088/1674-1056/abd9b4

Quantum plasmon enhanced nonlinear wave mixing in graphene nanoflakes

Hanying Deng(邓寒英), Changming Huang(黄长明), Yingji He(何影记), and Fangwei Ye(叶芳伟)
Chin. Phys. B, 2021, 30 (**4**): 044213. DOI: 10.1088/1674-1056/abea8d

Modulation and enhancement of photonic spin Hall effect with graphene in broadband regions

Peng Dong(董鹏), Gaojun Wang(王高俊), and Jie Cheng(程杰)
Chin. Phys. B, 2021, 30 (**3**): 034202. DOI: 10.1088/1674-1056/abccb2

Plasmonic characteristics of suspended graphene-coated wedge porous silicon nanowires with Ag partition

Xu Wang(王旭), Jue Wang(王珏), Tao Ma(马涛), Heng Liu(刘恒), and Fang Wang(王芳)
Chin. Phys. B, 2021, 30 (**1**): 014207. DOI: 10.1088/1674-1056/abb65c

Tunable dual-band terahertz graphene absorber with guided mode resonances

Jun Wu(吴俊), Xia-Yin Liu(刘夏吟), and Zhe Huang(黄喆)
Chin. Phys. B, 2021, 30 (**1**): 014202. DOI: 10.1088/1674-1056/abaee2

Dynamic modulation in graphene-integrated silicon photonic crystal nanocavity*

Long-Pan Wang(汪陇盼)[1], Cheng Ren(任承)[1,†], De-Zhong Cao(曹德忠)[1], Rui-Jun Lan(兰瑞君)[1], and Feng Kang(康凤)[2]

[1] *School of Opto-Electronic Information Science and Technology, Yantai University, Yantai* 264005, *China*
[2] *Wenjing College, Yantai University, Yantai* 264005, *China*

(Received 29 September 2020; revised manuscript received 8 January 2021; accepted manuscript online 11 January 2021)

Silicon-based electro-optic modulators are the key devices in integrated optoelectronics. Integration of the graphene layer and the photonic crystal (PC) cavity is a promising way of achieving compact modulators with high efficiency. In this paper, a high-quality (Q) acceptor-type PC nanocavity is employed to integrate with a single-layer graphene for realizing strong modulation. Through tuning the chemical potential of graphene, a large wavelength shift of 2.62 nm and a Q factor modulation of larger than 5 are achieved. A modulation depth (12.8 dB) of the reflection spectrum is also obtained. Moreover, the optimized PC nanocavity has a large free spectral range of 131.59 nm, which can effectively enhance the flexibility of the modulator. It shows that the proposed graphene-based PC nanocavity is a potential candidate for compact, high-contrast, and low-power absorptive modulators in integrated silicon chips.

Keywords: graphene, photonic crystal nanocavity, tunable

PACS: 42.70.Qs, 42.82.Gw, 42.25.Bs **DOI:** 10.1088/1674-1056/abda2b

1. Introduction

Electro-optic modulators and switches are fundamental devices in optoelectronic integrated circuits.[1–4] Meanwhile, the most critical issue is whether the conversion of photo-electric signal can be realized effectively through modulators. Strong electro-optic modulation materials are needed to achieve compact and efficient modulators. Graphene,[5–8] a two-dimensional (2D) material with linear dispersion at the Dirac point, is an attractive candidate because of its excellent properties, such as tunable chemical potential and high carrier mobility, achieved by applying an electric field. Owing to these advantages, graphene can be used in integrated photonics based on silicon,[9–17] which is a promising candidate for on-chip data transmission. Through covering silicon devices with monolayer or multilayer graphene, tunable electro-optic modulators can be realized by the electrical gating of graphene by the use of an electrolyte.

In general, the size of electro-optic modulator based on silicon waveguide integrated with graphene[13–15] is relatively large because light needs to travel a considerable distance to realize the coupling of graphene with waveguide effectively. A planar PC nanocavity with a high quality factor is used to integrate with graphene to further enhance the light–matter interaction and reduce the size of the device.[18–22] Resonant modes can be strongly confined within the PC cavity region due to the effect of PC band gap. The evanescent field of resonant mode will strongly interact with the graphene layer when the silicon PC cavity is covered with graphene layer. Then, the modulation of cavity modes can be achieved by changing the electrical gating of graphene layer.

Majumdar *et al.* first realized the electrical control of the graphene–cavity system and about 2-nm shift of the cavity resonant linewidth was observed.[18] However, less than 1-nm shift of the resonant cavity mode was realized. Gan *et al.* reported a resonance wavelength shift close to 2 nm and Q factor modulation of more than 3 when integrating an air-slot PC nanocavity with graphene.[19] Three cavity modes were introduced in the near-infrared wavelength range, which reduced the free spectrum range (FSR). Chiba and Notomi proposed a reconfigurable nanocavity in a graphene-loaded silicon PC waveguide; a maximum resonant wavelength shift of about 0.5 nm was achieved.[20]

A large resonant wavelength shift can effectively reduce the restriction on the requirement of a high-Q cavity, *i.e.* a narrow linewidth of the cavity mode, which is conducive to resolving the two peaks before and after the modulator is excited by the electric field. Moreover, a large FSR means a single resonance in an ultra-wide band without being affected by adjacent resonances, which is especially attractive in an integrated wavelength division multiplexing system. Therefore, considering practical applications, the modulation wavelength shift and FSR must be maximized.

In this paper, we propose a high-Q acceptor-type PC

*Project supported by the National Natural Science Foundation of China (Grant No. 11674273) and the Science and Technology Plan Projects of Colleges and Universities of Shandong Province, China (Grant No. J15LJ52).

†Corresponding author. E-mail: cren@ytu.edu.cn

© 2021 Chinese Physical Society and IOP Publishing Ltd

nanocavity coupled with graphene layer in 2D silicon slabs. Through regulating the chemical potential of graphene, the resonance wavelength shift reaches 2.62 nm, which is a relatively large voltage tuning result compared with the findings reported thus far. A large modulation depth of 12.8 dB for the light reflection can also be obtained. The Q factor can be reduced from the order of 10^4 to about 300. Furthermore, only one resonant mode exists in the near-infrared band (1500 nm–1640 nm), and a large FSR (131.59 nm) can be achieved.

The rest of this paper is organized as follows. In Section 2, we propose an acceptor-type PC nanocavity and then optimize its performance. Section 3 shows the modulation characteristics of the optimized nanocavity integrated with a graphene layer. Finally, Section 4 summarizes the study.

2. Design and optimization of PC nanocavity

The 2D triangular-lattice PC consists of circular air holes etched in a 220-nm thick silicon membrane on an insulator (SOI) wafer, whose process is compatible with the current complementary metal–oxide–semiconductor process. Meanwhile, the lattice constant a is 450 nm, and the radius of air holes is 120 nm ($0.267a$). The refractive index of the membrane silicon is set to be 3.45 for the near-infrared light around 1550 nm. The well-established three-dimensional (3D) plane-wave expansion method is used to calculate the band structure of the above PC slab. In simulations, 30 pixels per lattice constant a together with periodic boundary conditions are used to ensure the calculation accuracy. The PC slab exhibits a 2D band gap of TE-like polarization ranging from 1402 nm to 1684 nm.

The traditional way to construct a defect cavity is to miss an air hole in the center of PC slab to realize a usual L1 (missing one air hole) nanocavity. Then, six nearest-neighbor air holes around the defect column are eliminated, corresponding to an L7 (missing seven air holes) nanocavity. This condition is equivalent to filling seven air holes with the background silicon. Subsequently, an air hole with radius R_a is inserted in the center of L7 cavity, and an A1 cavity, which is an acceptor-type cavity, is formed. Figure 1 shows the schematic of the A1 cavity.

The major difference between the A1 cavity and traditional L7 cavity lies in the occupation material within the center of the cavity. The material in the center of L7 nanocavity is silicon. On the contrary, the core of A1 nanocavity is air or infiltrated with other nonlinear materials. When the A1 cavity is in resonance, the resonant mode will have strong interaction with air or other nonlinear materials. Therefore, the A1 cavity may present a better modulation effect than traditional L-type cavity when the cavity is integrated with other nonlinear materials.

The high Q factor indicates that the nanocavity has good localizing characteristics to light, which is conducive to enhancing the interaction between the light field and material. Usually, the Q factor of the original A1 cavity is lower than that of traditional L3 cavity as described in Ref. [23]. Therefore, the A1 cavity needs to be optimized to achieve a moderate Q factor. The radius R_a of central air hole and the positions of neighboring holes around the cavity need to be changed to improve the performance of the A1 cavity.

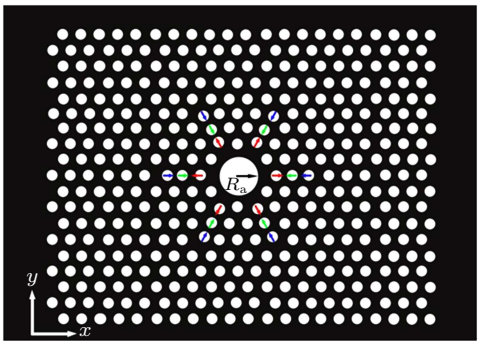


Fig. 1. Schematic diagram of A1 cavity in triangular-lattice PC slab, where R_a is radius of central air hole, with red, green, and blue arrows representing the first, second, and third nearest-neighbor air holes along Γ–K direction, respectively, and arrows pointing to the direction of displacement.

As described in Ref. [24], changing the positions or shapes of air holes near the cavity edge can make the electric field profile of the cavity mode closer to the Gaussian function, thus obtaining a high Q factor for L3 cavity. However, the optimization of the A1 cavity needs to be further explored. Based on the above consideration, we first change the radius R_a of the central air hole to optimize the performance of A1 cavity. The 3D finite-difference time-domain (FDTD) combined with Pade approximation method is used to calculate the Q factor and resonant wavelength of the cavity. In simulations, 30 pixels per lattice constant a together with Berenger's perfectly matched layer boundary conditions are used for ensuring the calculation accuracy. Point sources with broad spectrum are placed at the asymmetric positions in the cavity region to excite the cavity modes. Figure 2 shows the calculated results as a function of radius R_a. The black line with solid squares in Fig. 2 shows the relationship between Q factor and R_a, where R_a is changed from $0.5a$ to $1.15a$. The Q factor first increases and then decreases with the increase in R_a. When R_a equals $0.917a$, the Q factor of A1 cavity reaches a maximum value of 17232, achieving over four orders of magnitude.

With the increase in R_a, the effective refractive index near the cavity region decreases. Thus, the resonant wavelength of the cavity moves to the short-wavelength range. The red line with solid circles in Fig. 2 shows the calculated relationship between the resonant wavelength and R_a. The resonant wavelength is 1548.41 nm when R_a is $0.917a$. When R_a is changed from $0.764a$ to $0.987a$, the resonant wavelength of the cavity can be located within a range of 1500 nm–1640 nm.

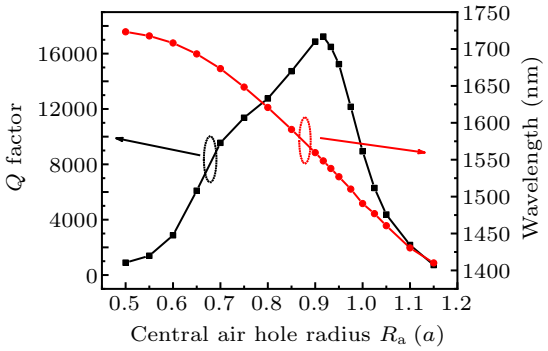


Fig. 2. Calculated Q factor and resonant wavelength versus central air hole radius R_a.

Second, we displace the six air holes at position A (the nearest neighbors) (red arrows in Fig. 1) outwards in the Γ–K direction ranging from 0a to 0.30a. All the displacements are parallel to the lattice vector, whereas $R_a = 0.917a$ is kept unchanged. Figure 3(a) shows the calculated results as a function of air hole shift. As the air holes are displaced outwards from 0a to 0.30a, the Q factor increases significantly and then decreases (black line with solid squares in Fig. 3(a)). The maximum Q factor, which is as large as 26962, is obtained from the air hole shift at position A of 0.05a. In Fig. 3(a), the red line with solid circles represents the variation in resonant wavelength of A1 cavity. When the shift amplitude ranges from 0a to 0.30a, the resonant wavelength can be monotonically increased from 1548.41 nm to 1615.82 nm, and the wavelength-tuning magnitude can be increased up to 67 nm. The resonant wavelength of A1 cavity is 1566.44 nm when the peak Q factor is obtained for air hole shift of 0.05a at position A.

Third, we shift the six air holes at position B (the second nearest neighbors) (green arrows in Fig. 1) inwards along the Γ–K direction from 0a to 0.30a. All the displacements are parallel to the lattice vector, with the air holes fixed at position A at the optimal outward displacement of 0.05a. In Fig. 3(b), the black line with solid squares and red line with solid circles correspond to the calculated Q factors and resonant wavelengths, respectively. The maximum Q factor, which is as large as 29150, is achieved for the inward displacement of 0.05a of air hole B. Moreover, the resonant wavelength of A1 cavity is 1565.42 nm. Given that the air hole at position B is at the periphery of the A1 cavity, displacement of air hole B has less effect on the cavity mode than that of air hole A. Therefore, the wavelength shift is 4.8 nm.

Moreover, we shift the six air holes at position C (the third nearest neighbors) (blue arrows in Fig. 1) inwards in a manner similar to that of B, with the positions of air holes A and B fixed at their optimal values, that is, outward 0.05a and inward 0.05a, respectively. The results are shown in Fig. 3(c). The maximum Q factor of 30171 is obtained for the displacement of air hole C of 0.20a. The corresponding resonant wavelength is about 1565.42 nm. In addition, when shifting the air holes at position C inwards from 0a to 0.30a, the resonant wavelength of A1 cavity remains almost unchanged. This result may be caused by the location of air holes at position C at the outer periphery of A1 cavity. Meanwhile, the movements of air holes have minimal effect on resonance wavelength.

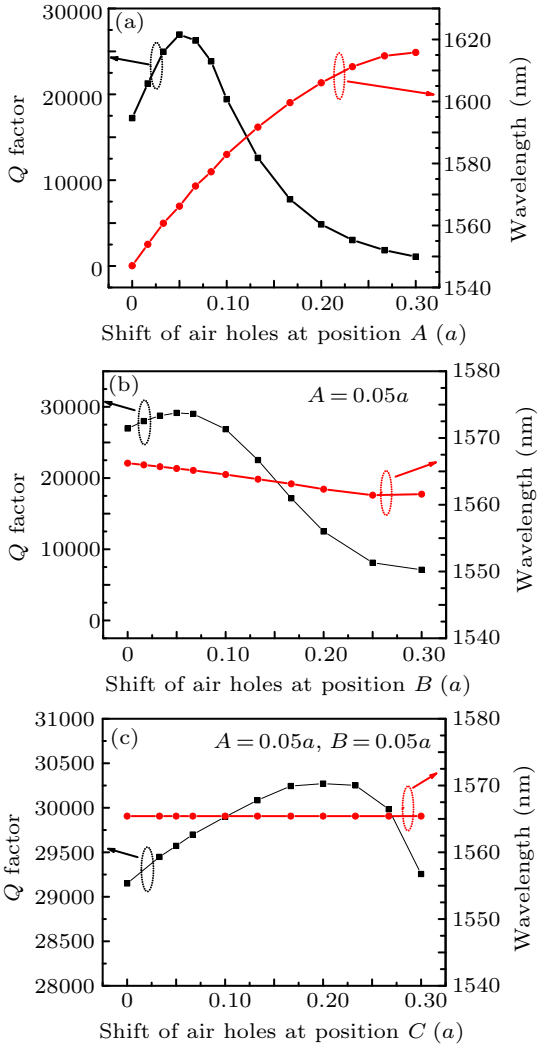


Fig. 3. (a) Q factors and resonant wavelengths obtained by FDTD simulations for A1 cavities with a range of displacements of air holes at (a) position A (the nearest neighbors), (b) position B (the second nearest neighbors) with the air holes fixed at position A at the optimal outward displacement of 0.05a, and (c) position C (the third nearest neighbors), with the positions of air holes A and B fixed at their optimal values, that is, outward 0.05a and inward 0.05a, respectively.

Figure 4 shows the electric field distribution of the optimized A1 cavity at 1565.42 nm. The red color represents the range with a strong amplitude, whereas the blue color denotes the range with a weak amplitude. It is shown in Fig. 4 that the electric field is mainly localized at the edge of the cavity, where strong interaction occurs when the nonlinear material is filled.

Although a considerably high Q factor can be obtained for the traditional L-type PC nanocavity,[25] the nanocavity with a moderate Q factor is necessary for modulation devices integrated with graphene, which can achieve a relatively large spectral bandwidth. The Q factor of graphene-based PC

nanocavity, measured by cross-polarized reflectivity measurement setup, is only several hundreds.[18,19] Therefore, the performance of the optimized A1 cavity is sufficient for the use in modulation devices integrated with graphene.

Moreover, in the whole photonic band gap (1402 nm–1684 nm) of TE-like polarization, two resonant peaks, 1433.83 nm and 1565.42 nm, are observed for the optimized A1 cavity. Figure 5 shows the calculated transmission spectrum, in which a large FSR of 131.59 nm can be achieved. In the FDTD simulations, a broad spectrum Gaussian pulse with a width of $4a$ in the y direction is normally launched on the left side of the structure shown in Fig. 1. The time evolution of the pulse is collected by a power detector with a wider width of $6a$ on the right side of the structure, and then transformed to the frequency domain by Fourier transform. Finally, the transmission spectrum shown in Fig. 5 can be achieved by dividing the output power by the input power at each frequency. Other parameters are the same as those used in previous calculations.

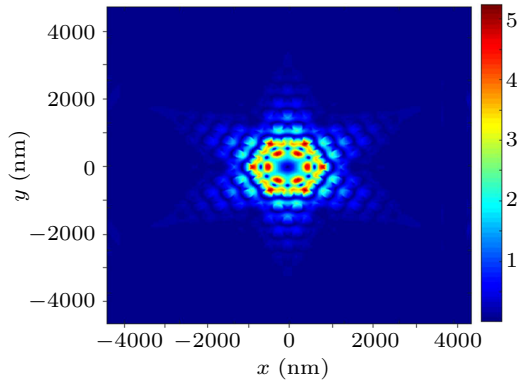


Fig. 4. Electric field distribution of the optimized A1 cavity at wavelength 1565.42 nm, where red color represents the range with strong amplitude, and the blue color denotes the range with weak amplitude.

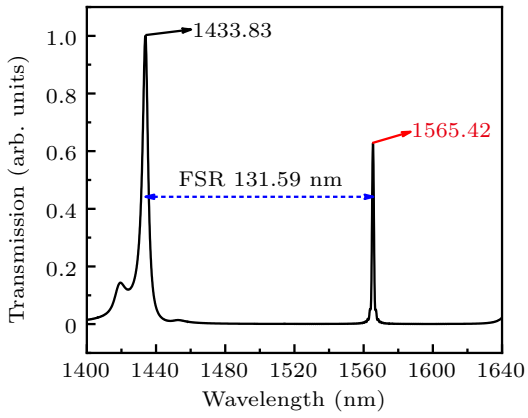


Fig. 5. Calculated transmission spectrum for structure shown in Fig. 1, showing two resonant peaks (1433.83 nm and 1565.42 nm) in the whole photonic band gap (1402 nm–1684 nm) of TE-like polarization.

3. Tunable PC nanocavity with single layer graphene

Graphene is a 2D crystal consisting of a single-layer carbon atoms and has intriguing optical absorption properties. The optical properties of graphene are directly related to its chemical potential, and its chemical potential can be controlled by applying a voltage to the graphene layer.[18,19]

The dielectric constant of graphene depends on the surface conductivity of single-layer graphene, which can be expressed as

$$\varepsilon = \varepsilon_0 + \mathrm{i}\frac{\sigma_{\mathrm{inter}} + \sigma_{\mathrm{intra}}}{t\omega}, \tag{1}$$

where σ_{intra} and σ_{inter} are the electrical conductivities determined by the intra-band transition and inter-band transition, respectively; ω is the angle frequency of light; ε_0 is the dielectric constant of vacuum; t is the thickness of graphene layer.

Based on Kubo formula, the graphene conductivity can be written as follows:[26]

$$\begin{aligned}&\sigma(\omega,\Gamma,\mu_{\mathrm{c}},T)\\ &= \sigma_{\mathrm{intra}}(\omega,\Gamma,\mu_{\mathrm{c}},T)+\sigma_{\mathrm{inter}}(\omega,\Gamma,\mu_{\mathrm{c}},T),\end{aligned} \tag{2}$$

$$\begin{aligned}&\sigma_{\mathrm{intra}}(\omega,\Gamma,\mu_{\mathrm{c}},T)\\ &= \frac{-\mathrm{i}e^2}{\pi\hbar^2(\omega+\mathrm{i}2\Gamma)}\int_0^{\infty}\varepsilon\left(\frac{\partial f_{\mathrm{d}}(\varepsilon)}{\partial\varepsilon}-\frac{\partial f_{\mathrm{d}}(-\varepsilon)}{\partial\varepsilon}\right)\mathrm{d}\varepsilon,\end{aligned} \tag{3}$$

$$\begin{aligned}&\sigma_{\mathrm{inter}}(\omega,\Gamma,\mu_{\mathrm{c}},T)\\ &= \frac{\mathrm{i}e^2(\omega+\mathrm{i}2\Gamma)}{\pi\hbar^2}\int_0^{\infty}\frac{f_{\mathrm{d}}(-\varepsilon)-f_{\mathrm{d}}(\varepsilon)}{(\omega+\mathrm{i}2\Gamma)^2-4(\varepsilon/\hbar)^2}\mathrm{d}\varepsilon,\end{aligned} \tag{4}$$

where Γ is the scattering rate, μ_{c} the chemical potential, and T the working temperature of graphene.

The Fermi–Dirac function $f_{\mathrm{d}}(\varepsilon)$ contains the chemical potential information μ_{c}, which can be expressed as

$$f_{\mathrm{d}}(\varepsilon) = \frac{1}{\exp((\varepsilon-\mu_{\mathrm{c}})/(k_{\mathrm{B}}T))+1}. \tag{5}$$

Therefore, the dielectric constant and electrical conductivity of graphene can be tuned by changing the chemical potential. Figures 6(a) and 6(b) show the imaginary part and real part of electrical conductivity of graphene as a function of chemical potential μ_{c}, which are shown by black line with solid squares and black line with solid circles, respectively. The real part of electrical conductivity represents absorption loss in a graphene layer. Figure 6(b) shows that the real part of electrical conductivity decreases gradually with the increase of chemical potential, corresponding to the reduced absorption loss of graphene. These are derived by assuming $T = 300$ K and $\omega = 2\pi c/\lambda$ ($\lambda = 1550$ nm). As for the scattering rate Γ of graphene, we consider 100 fs, corresponding to a typical value for graphene at room temperature.

We use the monolayer graphene to cover the A1 nanocavity. Figure 7 shows the schematic diagram of electrically controlled graphene-PC nanocavity. Meanwhile, the drain, source, and gate electrodes of the graphene field-effect transistor (FET) are denoted as D, S, and G in Fig. 7, respectively. The top magenta layer is the monolayer graphene. Underneath the graphene layer, is the air-bridge PC A1 nanocavity etched

on 220-nm silicon membrane. This design can further enhance the coupling rate between graphene layer and A1 cavity modes because the cavity modes can experience more overlapping with the graphene layer than the traditional L3 cavity.

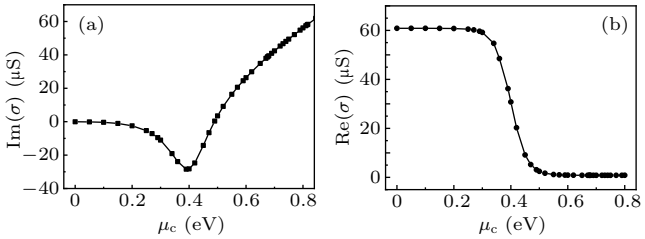


Fig. 6. Calculated electrical conductivity of graphene as a function of chemical potential μ_c, with panels (a) and (b) representing imaginary part and real part of electrical conductivity, respectively.

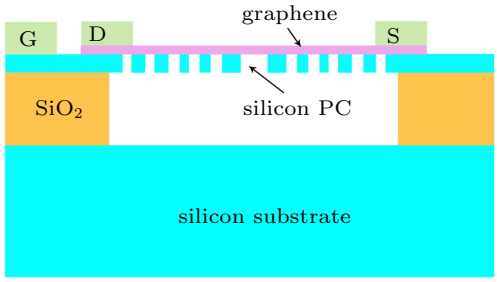


Fig. 7. Schematic diagram of PC cavity–graphene device, where A1 cavity is fabricated on a 220-nm thick silicon membrane on SOI wafer, D, S, and G denote drain, source, and gate electrodes of graphene FET, respectively.

Based on the above theoretical analysis, the dielectric constant of graphene is a function of its chemical potential μ_c. Therefore, the resonant wavelength of the A1 nanocavity covered with graphene can be tuned by adjusting the chemical potential μ_c of graphene. The reflection spectra of the integrated structure are simulated with the FDTD method. In the simulations, a dipole source with broad spectrum is placed in the center of A1 nanocavity and a power detector in the out-of-plane free space above the PC cavity is used to collect the emission power. The calculation parameters are the same as those used in the previous calculations. Figure 8 shows the resonant wavelength of the calculated reflection spectra when the chemical potential μ_c changing from 0 eV to 0.8 eV.

The resonant wavelength of the cavity can be divided into four ranges according to the changes in chemical potential μ_c. In the first range, the change in resonant wavelength is extremely small, almost kept at about 1564.43 nm, when the chemical potential changing from 0 eV to 0.20 eV. In the second range, the resonant wavelength increases monotonically to 1565.3 nm, *i.e.* the wavelength shifts 0.87 nm, when the chemical potential is adjusted from 0.20 eV to 0.39 eV. In the third range, when the chemical potential is between 0.39 eV and 0.74 eV, the change in resonant wavelength shows complexity. The resonant wavelength decreases monotonically from 1565.3 nm to 1563.34 nm when the chemical potential increases from 0.39 eV to 0.6 eV. However, when the chemical potential changes from 0.6 eV to 0.74 eV, the resonance wavelength increases monotonically and then decreases to 1562.68 nm. Meanwhile, the resonant wavelength reaches a minimum value of 1562.68 nm when the chemical potential is 0.74 eV, *i.e.*, the wavelength shift can reach 2.62 nm when the chemical potential is in the third range (0.39 eV to 0.74 eV). Finally, when the chemical potential is tuned from 0.74 eV to 0.80 eV, the resonant wavelength can increase rapidly from 1562.68 nm to 1565.3 nm, *i.e.*, the resonant wavelength shift is also 2.62 nm. Meanwhile, the resonant wavelength reaches a maximum value of 1565.3 nm when the chemical potential is 0.77 eV. In summary, the maximum tuning range of the resonance wavelength can reach 2.62 nm, which is a relatively large value for electrically tuned PC-cavity modulators to our knowledge. In addition, compared with the resonance wavelength of A1 cavity without graphene, the resonant wavelength of the cavity covered with graphene moves to a short value.

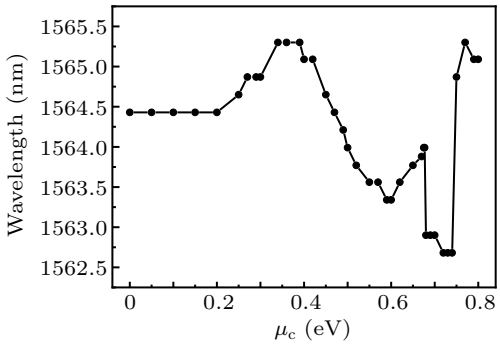


Fig. 8. Resonant wavelength of optimized A1 nanocavity integrated with single-layer graphene when chemical potential μ_c changing from 0 eV to 0.8 eV.

In addition, changing the complex dielectric constant or the real part of conductivity of graphene (which represents absorption loss in a graphene) can tune the Q value of the A1 cavity covered with graphene. Figure 9 shows the calculated Q factor as a function of μ_c in a range from 0 eV to 0.8 eV. The Q factor increases with chemical potential μ_c increasing, which corresponds to the gradual decrease of the real part of electrical conductivity of graphene shown in Fig. 6(b). The decreasing of absorption loss of graphene means that the Q factor of A1 nanocavity is improved.

Comparing with the resonance behavior of optimized A1 cavity without graphene, an evident degradation of Q factor occurs due to the absorption of graphene layer. Two saturation-like ranges and a fast modulation range are observed in the whole range. In the first saturation-like range, *i.e.*, in a chemical potential range from 0 eV to 0.30 eV, the Q factor of the cavity increases slightly and stays at about 340. In the second saturation-like range, *i.e.*, in the chemical potential (μ_c) in a range from 0.55 eV to 0.8 eV, the Q factor shows a small fluctuation and is kept at about 1850. Meanwhile, the maximum Q factor is about 1892 when the μ_c is 0.65 eV. The

Q factor increases rapidly from about 340 to 1850 when the chemical potential μ_c is in the fast-modulation range (0.30 eV to 0.55 eV). In the above region, the maximum modulation amplitude for Q factor can be in excess of 5.

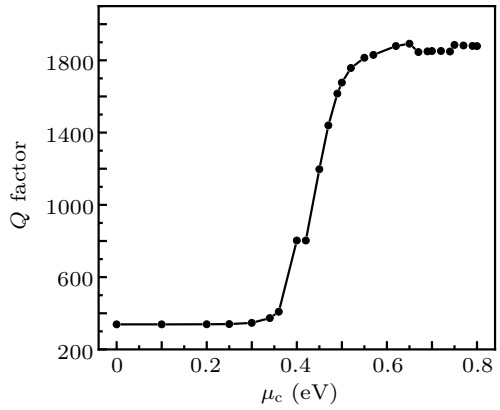


Fig. 9. The Q factor of graphene-PC cavity when changing the chemical potential μ_c from 0 eV to 0.8 eV.

To better understand the modulation on cavity modes, we calculate the reflection spectra of A1 cavity integrated with graphene for different chemical potentials. Figure 10 shows the calculated results when the chemical potentials are 0.2, 0.4, 0.5, 0.6, and 0.7 eV, corresponding to the magenta solid, black solid, green dashed–dotted, blue dashed, and red dotted lines, respectively. When the chemical potentials are equal to 0.7 eV and 0.6 eV, the peak reflectivity and linewidth of two cavity modes are similar except for the difference in resonant wavelengths, that is, 1562.76 nm and 1563.34 nm, respectively. However, when the chemical potentials are equal to 0.5 eV and 0.4 eV, which are located in the fast-modulation range, a significant broadening in the cavity linewidth and a decrease in the peak reflectivity can be observed with the decreased chemical potential of graphene. Simultaneously, the resonant wavelengths are 1563.99 nm and 1565.3 nm, corresponding to chemical potentials of 0.5 eV and 0.4 eV, respectively. In addition, when the chemical potential is equal to 0.2 eV, located in the first saturation-like range, the peak reflectivity decreases significantly. As depicted in Fig. 10, the modulation depth is as large as $\sim$ 12.8 dB, when the chemical potential is changed from 0.7 eV to 0.2 eV.

Table 1 displays the comparisons of the proposed modulator based on A1 cavity with other PC modulators reported previously. As shown in Table 1, our designed modulator has the highest modulation efficiency in the several previously reported PC modulators.

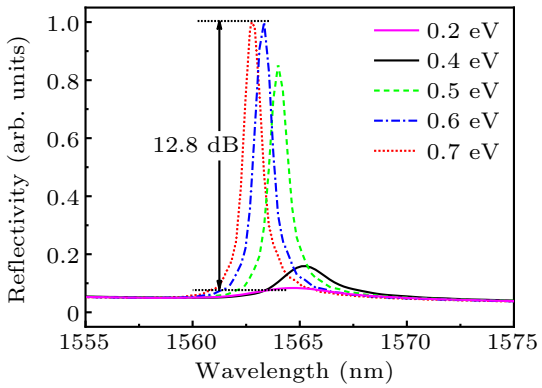


Fig. 10. Reflection spectra of graphene PC cavity when chemical potentials are 0.2, 0.4, 0.5, 0.6, and 0.7 eV, corresponding to magenta solid, black solid, green dashed–dotted, blue dashed, and red dotted lines, respectively.

Table 1. Comparisons of proposed modulator with various PC modulators.

References	Types of PC devices	Wavelength shift	Modulation depth	FSR	Q-factor modulation
[18]	L3 cavity	1 nm	6 dB	No	300–700
[19]	air-slot cavity	2 nm	10 dB	17 nm	300–1100
[27]	nanobeam cavity	0.95 nm	12.5 dB	125.6 nm	1700–25000
[20]	waveguide cavity	0.5 nm	No	No	10^5–10^6
Our work	A1 cavity	2.62 nm	12.8 dB	131.59 nm	300–1800

4. Conclusions

In summary, we have designed a novel acceptor-type A1 cavity in 2D silicon PC slabs. The Q factor can achieve over four orders of magnitude, which is conducive to producing a strong interaction between cavity mode and other material. Through changing the chemical potential of graphene on the top of A1 cavity, the resonant wavelength can be tuned from 1562.68 nm to 1565.30 nm, *i.e.*, the maximum wavelength shift is about 2.62 nm. Moreover, the Q factor can be changed from a peak value of 1892 to about 340, and the maximum modulation factor exceeds five due to the strong optical modulation. Therefore, the resonant wavelength and Q factor can be strongly tuned simultaneously for our proposed A1 cavity with a moderate Q factor. This work shows that such a graphene-cavity-based modulator can be used for implementing the fast and intense electro-optic modulation in integrated silicon photonic applications.

References

[1] Chen L, Preston K, Manipatruni S and Lipson M 2009 *Opt. Express* **17** 15248

[2] Tanabe T, Nishiguchi K, Kuramochi E and Notomi M 2009 *Opt. Express* **17** 22505

[3] Shakoor A, Nozaki K, Kuramochi E, Nishiguchi K, Shinya A and Notomi M 2014 *Opt. Express* **22** 28623
[4] Pospischil A, Humer M, Furchi M M, Bachmann D, Guider R, Fromherz T and Mueller T 2018 *Nature* **562** 101
[5] Hanson G W 2008 *J. Appl. Phys.* **103** 064302
[6] Stauber T, Peres N M R and Guinea F 2007 *Phys. Rev. B* **76** 205423
[7] Falkovsky L A 2008 *J. Phys.: Conf. Ser.* **129** 012004
[8] Tan Y W, Zhang Y, Bolotin K, Zhao Y, Adam S, Hwang E H, Sarma S D, Stormer H L and Kim P 2007 *Phys. Rev. Lett.* **99** 246803
[9] Pospischil A, Humer M, Furchi M M, Bachmann D, Guider R, Fromherz T and Mueller T 2013 *Nat. Photon.* **7** 892
[10] Qiu C, Gao W, Vajtai R, Ajayan P M, Kono J and Xu Q 2014 *Nano Lett.* **14** 6811
[11] Du W, Li E P and Hao R 2014 *IEEE Photon. Technol. Lett.* **26** 2008
[12] Hu Y, Pantouvaki M, Campenhout J V, Brems S, Asselberghs I, Huyghebaert C, Absil P and Thourhout D V 2016 *Laser Photon. Rev.* **10** 307
[13] Liu M, Yin X, Ulin-Avila E, Geng B, Zentgraf T, Ju L, Wang F and Zhang X 2011 *Nature* **474** 64
[14] Ye S W, Yuan F, Zou X H, Shah M K, Lu R G and Liu Y 2017 *IEEE J. Sel. Top. Quantum Electron.* **23** 3400105
[15] Liu M, Yin X and Zhang X 2012 *Nano Lett.* **12** 1482
[16] Du L, Li Q, Li S, Hu, F, Xiong X, Li Y, Zhang W and Han J 2016 *Chin. Phys. B* **25** 027301
[17] Jiang R, Wu Z, Han Z and Jung H 2016 *Chin. Phys. B* **25** 106803
[18] Majumdar A, Kim J, Vuckovic J and Wang F 2013 *Nano Lett.* **13** 515
[19] Gan X, Shiue R, Gao Y, Mak K F, Yao X, Li L, Szep A, Walker D J, Hone J, Heinz T F and Englund D 2013 *Nano Lett.* **13** 691
[20] Chiba H and Notomi M 2019 *Opt. Express* **27** 37952
[21] Gan X, Mak K F, Gao Y, You Y, Hatami F, Hone J, Heinz T F and Englund D 2012 *Nano Lett.* **12** 5626
[22] Pan T, Qiu C, Wu J, Jiang X, Liu B, Yang Y, Zhou H, Soref R and Su Y 2015 *Opt. Express* **23** 23357
[23] Akahane Y, Mochizuki M, Asano T, Tanaka Y and Noda S 2003 *Appl. Phys. Lett.* **82** 1341
[24] Akahane Y, Asano T, Song B S and Noda S 2005 *Opt. Express* **13** 1202
[25] Asano T, Ochi Y, Takahashi Y, Kishimoto K and Noda S 2017 *Opt. Express* **25** 1769
[26] Du W, Hao R and Li E 2014 *Opt. Commun.* **323** 49
[27] Pan T, Qiu C, Wu J, Jiang X, Liu B, Yang Y, Zhou H, Soref R and Su Y 2015 *Opt. Express* **23** 23357